

Landscape-level vegetation classification and fractional woody and herbaceous vegetation cover estimation over the dryland ecosystems by unmanned aerial vehicle platform

Haozhou Wang^{a,b,c}, Dong Han^a, Yue Mu^{a,d}, Lina Jiang^a, Xueling Yao^a, Yongfei Bai^e, Qi Lu^a, Feng Wang^{a,*}

^a Institute of Desertification Studies, Chinese Academy of Forestry, Beijing, 100091, China

^b College of Biology and Environment, Nanjing Forestry University, Nanjing, Jiangsu, 210037, China

^c Faculty of Forestry and Environmental Management, University of New Brunswick, Fredericton, NB, E3B 5A3, Canada

^d Plant Phenomics Research Center, Nanjing Agricultural University, No. 1 Weigang, Nanjing, Jiangsu, 210095, China

^e State Key Laboratory of Vegetation and Environmental Change, Institute of Botany, The Chinese Academy of Sciences, Beijing, 100093, China

ARTICLE INFO

Keywords:

Dryland vegetation
Machine learning
Decision tree model
Digital orthophoto map
Otidic sandy land
Semi-arid ecosystem
Classification and regression tree (CART)

ABSTRACT

The change of fraction vegetation cover (FVC) is the key ecological index for vegetation dynamics of dryland ecosystem. However, it is difficult to directly map woody vegetation and herbaceous vegetation in the dryland from the satellite images due to the mixture of their distribution at small scale. Emerging UAV remote sensing provides a good opportunity to capture and quantify the distribution of the sparse vegetation in the drylands ecosystem. In this study, we proposed a new method to classify woody vegetation and herbaceous vegetation and calculate their FVC based on the high-resolution orthomosaic generated from UAV images by the machine learning algorithm of classification and regression tree (CART). This proposed method was validated and evaluated by visual interpretation, the detailed ground measurement dataset of 4832 trees and 18,798 shrubs and three popular machine learning algorithms of Support Vector Machine(SVM), Random Forest(RF), Gradient Boosting Decision Tree(GBDT). The overall assessments showed good overall accuracy (0.78), average accuracy (0.76), and the Kappa coefficient (0.64). The FVC of woody vegetation calculated from orthomosaic agreed well with that estimated from ground measurements. Both group of FVC have a stable linear relationship over different spatial scales. The proposed method showed higher efficiency of 166%, 111% and 290% than SVM, RF, GBDT respectively. A new optimized model was developed to reduce the workload of vegetation investigation and to design more efficient sampling strategies. The proposed method was incorporated into an interactive web-based software "UAV- High Resolution imagery Analysis Platform" (UAV-HIRAP, <http://www.uav-hirap.org>). Our study demonstrates that UAV-HIRAP combined with UAV platform can be a powerful tool to classify woody vegetation and herbaceous vegetation and calculate their FVC for sparse vegetation in the drylands. The new optimization model will inspire researchers to design more effective sampling strategies for future field investigation.

1. Introduction

Dryland covers about 45% of Earth's land surface and dryland ecosystem constitutes the largest biome on the planet (Schimel, 2010). Yet vegetation dynamics studies are dominated by other ecosystems, particularly the tropical forest with high biodiversity levels and high productivity, and the boreal forest with huge stocks of carbon. Drylands are less studied due to their low biodiversity level and sparse vegetation. Recent modeling studies have suggested that the trend and inter-

annual variability of the global carbon sink are driven by semi-arid ecosystems (Poulter et al., 2014; Ahlström et al., 2015). Therefore, long-term and continuous observations on semi-arid vegetation are essential for explaining the carbon cycle process and ecological dynamics in dryland ecosystems. However, investigation frequency and sample numbers based on field work are limited by available human labor and field time.

Conventional remote sensing techniques, e.g. satellite and manned aircraft, have been widely employed to monitor the dynamics of

* Corresponding author.

E-mail address: wangfeng@caf.ac.cn (F. Wang).

vegetation structure and function, e.g. coverage (Hansen et al., 2013), phenology (Jeong et al., 2017) and species distribution (Asner and Martin, 2009; Asner et al., 2017), over large extents for several decades. However, it is not well-suited to obtain the distribution, structure and function of sparse vegetation grown in dryland due to the low spatial resolution of satellite images and the high cost of airborne images. Besides, satellite and manned aircraft images are difficult to match with the detailed ground data due to overpass time and cloud contamination. Due to these limitations, a big challenge remains on how to collect a large number of high spatial-temporal resolution images of sparse vegetation in dryland ecosystems in a timely manner.

Recently, unmanned aerial vehicle (UAV) remote sensing, as an emerging tool, has provided a timely, high spatial resolution, and low-cost way of monitoring vegetation at the landscape scale (Anderson and Gaston, 2013). UAVs can assist researchers to generate ultra-fine grain landscape scale aerial photography such as Digital Orthophoto Map (DOM), Digital Elevation Model (DEM), Digital Terrain Model (DTM), Canopy Height Model (CHM), based on computer vision principles in hard-to-reach places (Leempoel et al., 2015; Cook, 2016; Malenovský et al., 2017). High spatial resolution vegetation images at landscape level are used to extract the structural and functional properties of vegetation and to explore the maintenance mechanism of biodiversity (Getzin et al., 2011; Hoffmann et al., 2016; McNeil et al., 2016; Zhang et al., 2016). In other studies, three-dimensional structure of individual plants can be obtained accurately by analyzing a large amount of digital images combined with ground control points (Cunliffe et al., 2016), and vegetation carbon storage were estimated based on allometry equations linked plant structure with biomass (Dandois and Ellis, 2013). The UAV is becoming an important tool in spatial ecology and environmental monitoring to obtain large amounts of observation data (Faye et al., 2016).

Image pattern recognition has been widely used in plant phenology observation (Guo et al., 2015; Filippa et al., 2016), plant phenotyping analysis (Duan et al., 2016), crop yield estimation (Yu et al., 2016), biodiversity assessment (Getzin et al., 2011) and gravels morphological characteristics determination (Mu et al., 2018). Some researchers obtained the structural parameters of vegetation in small areas by using single images from a common digital camera and fisheye camera (Richardson et al., 2001; Lynch et al., 2015). However, the study of sparse vegetation in arid areas often requires ultra-fine grain orthomosaic images covering larger areas. The file sizes of these orthomosaic images originating from hundreds to thousands of UAV photos can amount to dozens of gigabytes (Wallace et al., 2016). Developing a novel, automatic UAV image-based analysis method is a currently challenging problem for field ecology, particularly precisely extracting the properties of vegetation structure.

The elm (*Ulmus pumila*) sparse forest grassland is a transition zone between forest and grassland in semi-arid sandy land in China, which is widely distributed in Otingdag Sandy Land, Horqin Sandy land, and Mu Us Sandy land of the Inner Mongolia, as shown in Fig. 1. The vegetation community of this ecotone is a natural response to the hydrological and meteorological processes in the ecosystem located in semi-arid sandy land (Rodríguez-Iturbe et al., 1999; D'Odorico et al., 2007). The vegetation type and spatial pattern play an important role in controlling the spatial and temporal changes of hydrological processes in the region. The change of vegetation structure, e.g. height, fraction vegetation cover (FVC), are the key index for the dynamics of dryland ecosystem. As well known, encroachment of shrub vegetation into grasslands is widely considered to be a mechanism of grasslands degradation. Therefore, monitoring of shrub and grass plants is also necessary for the resilient management of dryland ecosystem. Currently, it is difficult to directly capture the dynamics of woody vegetation and herbaceous vegetation in the dryland from the satellite images respectively due to the mixture of their distribution at small scale. Emerging UAV remote sensing provides a good opportunity to obtain and quantify the distribution of the woody vegetation and herbaceous vegetation on the

sparse forest grassland at landscape scale. Developing a rapid and precise method to extract the woody vegetation and herbaceous vegetation from the ultra-high-resolution UAV image will be greatly beneficial to map vegetation pattern and to monitor vegetation dynamic in dryland (Wang, 2017).

Therefore, our purpose in this study was to: 1) develop a high-resolution image-based method to classify woody vegetation and herbaceous vegetation and estimate their FVC by UAV and machine learning algorithm; 2) validate and evaluate the proposed method by comparing with visual interpretation, the detailed ground-based measurement dataset and three popular machine learning algorithms; 3) develop a simple model for optimizing the workload of vegetation investigation.

2. Materials and methods

2.1. The study area overview

The study area is located in the north-east of Otingdag Sandland, Inner Mongolia, northeastern China. The average elevation of this area is 1300 m. The annual average temperature of 1.8 °C, the extreme minimum temperature of -40 °C, the extreme maximum temperature of 37 °C. The average annual rainfall of 313.8 mm and summer precipitation takes over 68.3%. The common wind direction is west and northwest, and average annual wind speed is 4 m·s⁻¹. The soil is aeolian sandy soil. The typical vegetation is natural sparse elm (*Ulmus pumila*) forest, shrubs and grass (Fig. 1b and c). A long-term monitoring plot (1 km × 1 km, 42.96 N, 115.95E) in Elm Sparse FOrest Grassland Ecosystem (ESFOGE-Plot) is established by Institute of Desertification Studies, Chinese Academy of Forestry (CAF) and Institute of Botany, Chinese Academy of Science in 2012 (Fig. 1a and d). All the aerial and ground investigation were conducted in this ESFOGE-Plot in 2013.

This study area was divided into four hundred sample plots of 50 m × 50 m by total station (Topcon GTS-336). The intersections of the grid were marked with concrete piles as permanent ground control points (GCP). All of them were marked with tag numbers according to the horizontal and vertical coordinates.

2.2. Data sources

The aerial photograph was taken by the Canon EOS 5DMark II camera via the Fixed-Wing UAV called "LTBT-Surveying Eagle" in June 2013. Color Digital Orthophoto Map (DOM) and DEM of ESFOGE-Plot was produced by hundreds of original UAV aerial images according to Structure-from-Motion (SfM) photogrammetry (Snavely et al., 2008). Spatial resolution of the orthomosaic is 0.1 m / pixel (Fig. 2a).

The ground investigation was conducted by 49 volunteers from July to August 2013. The crown diameter, plant height and diameter at breast height (DBH) of each tree and each shrub in the ESFOGE-Plot were measured by manual. At the same time, the location of each plant in each sample plot was measured in the user-defined coordinate system (the origin of the coordinate system is the lower left corner of the ESFOGE-Plot, X-axis in the west-east direction, Y-axis in the south-north direction, as shown in Fig. 1d). The accuracy of coordinate value is 0.1 m. The location of each tree and each shrub was measured by total station. There were 4832 elm trees and 18,798 shrubs of 14 different species in the ESFOGE-Plot.

A plant map was produced by using the trees' locations, long and short crown axis of tree crown. The shape of the tree crown is assumed to be a standard ellipse. The center points were tree location, and transverse/conjugate diameters were long/short crown diameters, respectively. The color of trees and shrubs in the plant map were red and blue, respectively. The plant map was implemented by Python PIL (Pillow) package (Ver. 4.2.1).

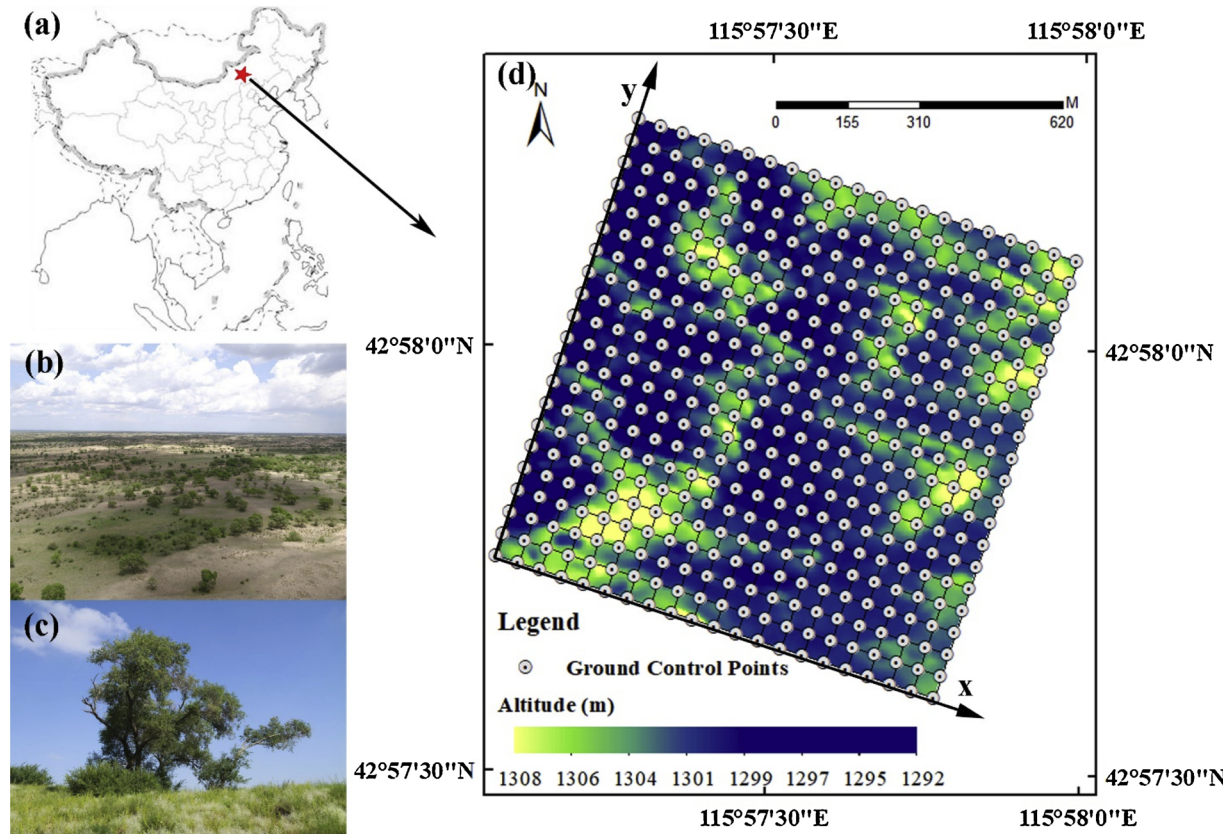


Fig. 1. Geographic location (a) and landscapes (b, c) of the long-term monitoring plot (42.96° N, 115.95° E) in Elm (*Ulmus pumila*) Sparse FOrest Grassland Ecosystem (ESFOGE-Plot). (d) Digital Elevation Model (DEM) derived from UAV images. There are 441 permanent ground control points in the plot. The size of ESFOGE-Plot is $1\text{ km} \times 1\text{ km}$. The UAV images were taken on 9 June 2013. The ground investigation was carried out from July to August 2013.

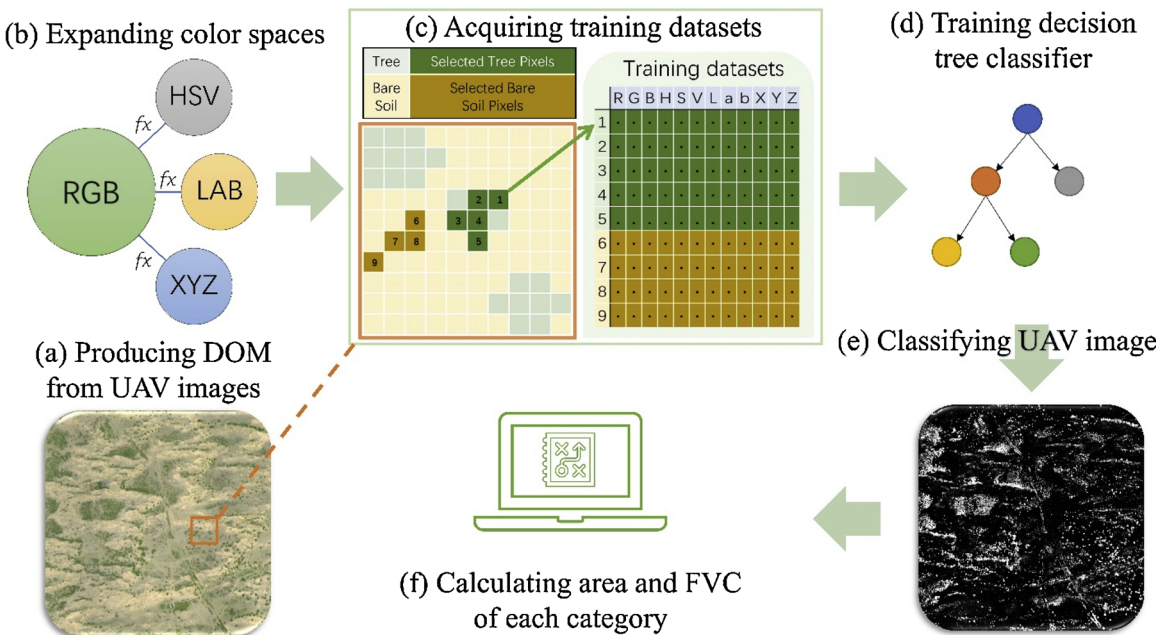


Fig. 2. Schematic workflow of vegetation classification and FVC calculation by using classification and regression tree (CART) algorithm. (a) producing color Digital Orthophoto Map (DOM) of the plot of Elm (*Ulmus pumila*) Sparse FOrest Grassland Ecosystem (ESFOGE-Plot) from UAV images; (b) expanding color space into HSV, $L^*a^*b^*$, and XYZ from RGB by using the color space transformation functions; (c) acquiring the pixels of tree & shrub, grass and bare sandy land as the training data set in the orthomosaic (DOM) derived from UAV; (d) training the model to create a decision tree classifier using the training data set; (e). classifying trees, shrubs, grass and bare sandy land using the classifier produced; (f) calculating the area and fractional vegetation cover (FVC) of woody vegetation, herbaceous vegetation and bare sandy land.

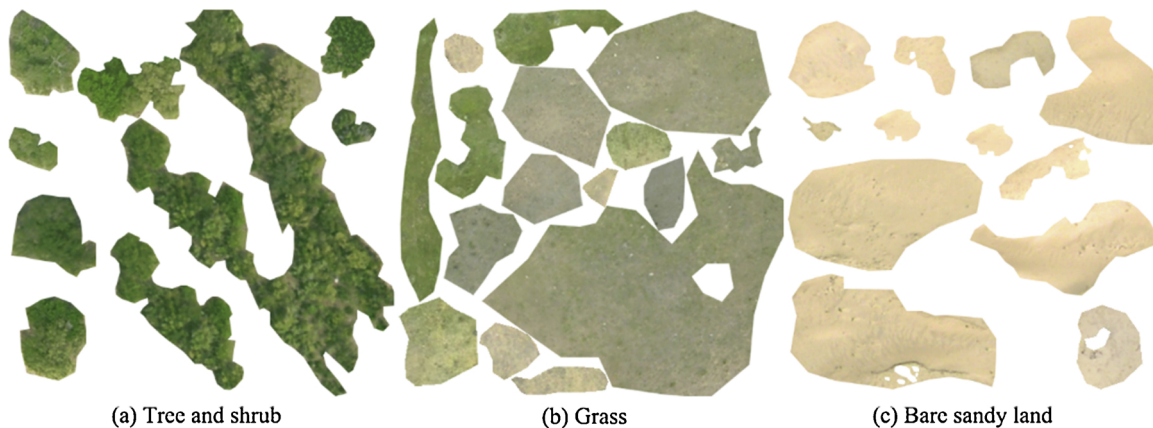


Fig. 3. The training dataset acquired by manual selection of the Region of Interest (ROI) on the orthomosaic derived from UAV, including (a) tree and shrub, (b) grass and (c) bare sandy land.

2.3. Woody vegetation and herbaceous vegetation classification and their FVC calculation

The classified model proposed in this paper was originated from Classification and Regression Tree (CART) algorithm (Breiman et al., 1984). Vegetation types were detected on the high resolution UAV images by coupling CART algorithm with the color spaces transformation function. The entire process of the proposed method includes the following five steps, 1) preparing the high-resolution orthomosaic from UAV; 2) expanding color spaces; 3) acquiring training dataset; 4) training model and classifying the image; 5) calculating the area and FVC of different vegetation (Fig. 2). The whole algorithm were implemented in Python3.6 (Guido, 2018).

2.3.1. Expanding color spaces

Color space is an image description method using a set of values (three components in common), such as RGB (Red, Green, and Blue), HSV (Hue, Saturation, Value), XYZ (quantitative links between wavelengths distributions and physiologically perceived colors in human color vision), and L*a*b* (L for Lightness, a and b for the color components green-red and blue-yellow respectively). The first step in image processing is color space conversion (Reinhard et al., 2001). We created 12-dimensional color features by expanding color space into HSV, XYZ, and L*a*b* from RGB information originated from DOM by using the color space reverse functions. Compared to three-dimensional information provided by RGB color spaces, twelve-dimensional information from four kinds of color space can provide addition information for training decision tree model. The HSV, XYZ, and L*a*b* color spaces were transformed from RGB information of original images.

The method of converting RGB to HSV was described in Eqs. (1) and (2). Maximum, minimum, and chroma component values were defined as max, min, and C, respectively (Hanbury and Serra, 2002).

$$\begin{cases} \text{Max} = \max(R, G, B) \\ \text{min} = \min(R, G, B) \\ C = \text{Max} - \text{min} \end{cases} \quad (1)$$

$$H = 60^\circ \times \begin{cases} \text{undefined}, & (\text{if } C = 0) \\ \frac{G - B}{C} \bmod 6, & (\text{if } \text{Max} = R) \\ \frac{B - R}{C} + 2, & (\text{if } \text{Max} = G) \\ \frac{R - G}{C} + 4, & (\text{if } \text{Max} = B) \end{cases}$$

$$S = \begin{cases} 0(V = 0) \\ \frac{C}{V}(V \neq 0) \end{cases}$$

$$V = M \quad (2)$$

The method on conversing RGB to XYZ is described in Eq. (3) (Fairman et al., 1997):

$$\begin{bmatrix} X \\ Y \\ Z \end{bmatrix} = \frac{1}{b_{21}} \begin{bmatrix} b_{11} & b_{12} & b_{13} \\ b_{21} & b_{22} & b_{23} \\ b_{31} & b_{32} & b_{33} \end{bmatrix} \begin{bmatrix} R \\ G \\ B \end{bmatrix}$$

$$= \frac{1}{0.17697} \begin{bmatrix} 0.49 & 0.31 & 0.2 \\ 0.17697 & 0.8124 & 0.01063 \\ 0 & 0.01 & 0.99 \end{bmatrix} \begin{bmatrix} R \\ G \\ B \end{bmatrix} \quad (3)$$

The method on conversing RGB to L*a*b* is described in Eqs. (4) and (5) (Schanda, 2007):

$$\begin{aligned} L^* &= 116 \times f\left(\frac{Y}{Y_n}\right) - 16 \\ a^* &= 500 \left(f\left(\frac{X}{X_n}\right) - f\left(\frac{Y}{Y_n}\right) \right) \\ b^* &= 200 \left(f\left(\frac{Y}{Y_n}\right) - f\left(\frac{Z}{Z_n}\right) \right) \end{aligned} \quad (4)$$

where

$$f(t) = \begin{cases} \sqrt[3]{t} (t > (\delta)^3) \\ \frac{t}{3 \times \delta^2} + \frac{4}{29} (t \leq (\delta)^3) \end{cases} \quad \delta = \frac{6}{29} \quad (5)$$

where, X_n , Y_n , and Z_n are the values of specific white object points.

2.3.2. Acquiring training dataset

The representative training sets of trees, shrubs, grass and bare sandy land were selected from the orthomosaic (DOM) by visual discrimination using common image editing software (e.g. GIMP, ImageJ, Photoshop etc.). The training dataset of different objects were shown in Fig. 3. In order to distinguish the white training dataset and the transparent background, the alpha layer of the PNG image was applied to make the background transparent rather than white. The transparent background was removed from the training dataset.

2.3.3. Training model and classifying the image

The CART algorithm was used to generate the decision tree model based on the training dataset acquired in the previous step. The training dataset of original RGB color information were expanded into 12 color features (R, G, B; H, S, V; X, Y, Z; L*, *a, *b) which were derived from the color space transformation functions described in Section 2.3.1. The generated decision tree model was applied to the plot orthomosaic (DOM). All the pixels in the orthomosaic were classified into three categories, i.e. woody vegetation, herbaceous vegetation and bare sandy land. Fractional cover (%) of each type vegetation were

calculated from the classified image by dividing the count of classified pixels in each category by the count of total pixels.

2.4. Software implementation

The proposed approach was developed into an interactive web-based software called “Unmanned Aerial Vehicles - High Resolution Imagery Analysis Platform” (UAV-HiRAP). It is accessible through the website <http://www.uav-hirap.org>. UAV-HiRAP was developed in Python-Flask website framework (Ver3.5.2).

2.5. Accuracy evaluation

The accuracy of the proposed method was evaluated by comparing with visual interpretation and ground measurement. Three common assessment parameter, i.e. average accuracy, overall accuracy, and Kappa coefficient were used to evaluate the accuracy of vegetation classification. FVC calculated by the proposed method were also compared against that calculated by ground measurement. Furthermore, we evaluated the impact of the subplots’ size on FVC estimation.

2.5.1. Classification accuracy assessment by visual interpretation

A 100 m × 100 m subplot including 1 million pixels in the ESFOGE-Plot was selected to assess the accuracy of the proposed methods by comparing machine classification with visual interpretation. The location of the sub-sample plot is shown in the black rectangle of Fig. 4. The selected region includes the features of different vegetation and sandy land in the study area. To be more specific: 1) The area of woody vegetation, herbaceous vegetation and sandy land are similar; 2) The crown shape size of tree and shrub range from small to large gradually. 3) It included grass with different density; 4) It included different types of bare sandy land. Tree, shrub and grass on the image were also marked by visual interpretation. The agreement of the machine classification and visual interpretation was assessed by the average accuracy (AA), overall accuracy (OA), and Kappa coefficient.

AA is the average of individual class accuracies. It is defined as follows:

$$\text{AA} = \frac{\sum_{i=0}^k \frac{n_i^c}{N_i}}{k} \quad (6)$$

Where k is the number of all categories, n_i^c is the number of correctly classified pixels in class i (diagonal number in error matrix), N_i is the total number of pixels in class i (diagonal number in error matrix), N is the total number of pixels in class i .

OA is an average of individual accuracies weighted by the size of

class samples. It is defined as follows:

$$\text{OA} = \frac{\sum_{i=0}^k \left(\frac{n_i^c}{N_i} \times N_i \right)}{N_p} = \frac{\sum_{i=0}^n n_i^c}{N_p} \quad (7)$$

Where N_p is the number of all pixels.

The Kappa coefficient is a measure of classification accuracy (Congalton, 1991). It is defined as follows:

$$\hat{\kappa} = \frac{N \times \sum_{i=1}^r x_{ij} - \sum_{i=1}^r (x_{i+} * x_{+j})}{N^2 - \sum_{i=1}^r (x_{i+} * x_{+j})} \quad (8)$$

Where, r is the number of rows in image matrix, $x_{i,j}$ is the pixel number which is classified as class i in the UAV image but be marked as class j in the reference image (i.e. image derived from virtual interpretation). $x_{i+} = \sum_j x_{i,j}$ means the pixel number which is classified as class i in image classification, and $x_{+j} = \sum_i x_{i,j}$ means the pixel number which is marked as class j in reference image. N is the total number of pixels (Bishop et al., 1975).

2.5.2. Evaluation between UAV-derived FVC and ground-derived FVC

To further evaluate the differences and accuracy between ground-based FVC and UAV image-based FVC, the FVC calculated from both methods were compared at different sampling spatial scales. ESFOGE-Plot was divided into 100, 400, 800 and 1600 grids at subplots side-lengths of 12.5 m, 25 m, 50 m, and 100 m respectively, as shown in the left corner of Fig. 6. The FVC values in each grid from both methods were compared at four sampling spatial scales. The agreement of both results was estimated based on the coefficients of determination (r^2 , calculated as the squared Pearson’s correlation coefficient) and the root mean square error (RMSE), where $\text{RMSE} = \sqrt{\frac{1}{n} \sum_i^n (FVC_i^{\text{UAV}} - FVC_i^{\text{Field}})^2}$.

2.6. An optimizing model for sampling design

In order to obtain the minimum number of sample plots while meeting the requirements of required precision before ground investigation, an optimizing model for size and minimum number of sample plots was developed based on the Monte-Carlo simulation (Landau and Binder, 2014). We calculated the deviations between FVC_0 (from the classified image of ESFOGE-Plot) and FVC_s (averaged from 1000 times stochastic sampling for sample plots with different side-length by Monte Carlo simulation) based on the classified images. The side-lengths of sample plots were changed from 1 m to 100 m in the simulation. The required minimum number of sample plots in ground

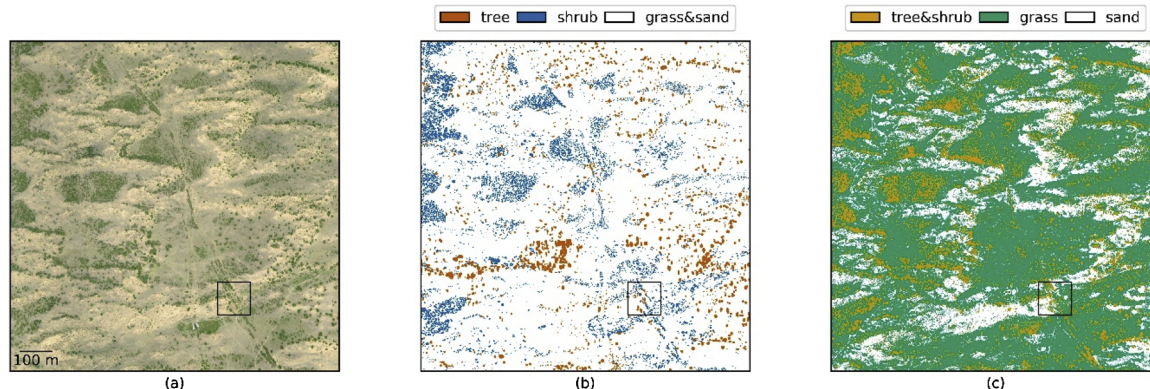


Fig. 4. The orthomosaic obtained from UAV, field measurements, and machine classification. (a) Digital Orthophoto Map (DOM) of the long-term monitoring plot of Elm (*Ulmus pumila*) Sparse Forest Grassland Ecosystem (ESFOGE-Plot), which was derived from the original UAV aerial images. Spatial resolution of the DOM image is 0.1 m/pixel, (b) woody vegetation map at individual scale shows the precise position and canopy diameter of each tree and each shrub (4832 elm trees and 18,798 shrubs), (c) woody vegetation and herbaceous vegetation image by machine classification. The area covered by a black box is the sample plot of 100 m × 100 m for validating the classification accuracy.

investigation were estimated from the optimizing model when the deviation between FVC_0 and FVC_s met the accuracy of 95% and 90% respectively.

The optimizing model represented the relationship between the side-length l and the required minimum number n of sub-quadrats in ground investigation, as shown in Eq. (9).

$$n = \frac{a}{(l + b)} \quad (9)$$

where a , b are coefficients, which are fitted from the group of the side-length l and minimum number n of sample plots calculated by stochastic simulation.

3. Results

3.1. Vegetation classification and FVC calculation

The orthomosaic image obtained from the UAV and the plant map derived from the ground measurements for ESFOGE-Plot were shown in Fig. 4a and b, respectively. The resolution of the color orthomosaic image was 0.1 m/pixel; it also has obvious color contrast among dark green woody (tree & shrub), gray-green grass, and yellow bare sandy land (Fig. 4a). The distribution of each tree and shrub are spatially explicit at individual scale on the plant map (red for trees and blue for shrubs, Fig. 4b).

The vegetation classification and FVC estimation were completed on the interactive website "UAV-HiRAP". Vegetation on the orthomosaic were classified into woody vegetation(tree & shrub), herbaceous vegetation (grass), and bare sandy land, as shown in Fig. 4c. Fig. 4 showed that vegetation distribution had a very good visual correspondence between UAV orthomosaic image (Fig. 4a), ground-derived plant map (Fig. 4b) and classified vegetation image (Fig. 4c).

The FVC of trees & shrub was estimated as 12.6%, which included 4.9% for trees and 7.7% for shrub based on the ground measurements (Table 1). However, it was hard to directly measure the FVC for all vegetation on the whole ESFOGE-Plot by the ground measurement, especially for herbaceous vegetation. Through the UAV-derived orthomosaic, the FVC of all vegetation was calculated as 80.3%, which includes trees & shrub of 14.1% and grass of 65.2%. Obviously, the FVC calculated by orthomosaic was higher than that estimated by the ground measurement.

3.2. Accuracy assessment and methods evaluation

3.2.1. Classification accuracy assessment

The accuracy of classification was assessed in the sub-plot of 100 m × 100 m, which included 1 million pixels (Fig. 5a). The validated result showed a good agreement between visual interpretation (Fig. 5b) and machine classification (Fig. 5c). Moreover, the machine learning algorithm captured the discrete pixels of the grass under the gap of trees crown, as shown in the magnified part in Fig. 5. Table 2 showed that the overall accuracy, average accuracy and Kappa coefficients of the proposed method were 77.7%, 76.3%, and 0.64. The numerical assessment demonstrated that the machine classification has good average accuracy and overall accuracy. The producer's accuracy and user's accuracy also demonstrated that the most of pixels are were

Table 1

Fractional vegetation cover (FVC) of tree, shrub, and grass by ground measurement and machine classification.

	Tree	Shrub	Grass
FVC_{field} (Fig5.b)	4.9%	7.7%	Null
	12.6%		
FVC_{UAV} (Fig5.c)	14.1%		65.2%
	80.3%		

classified correctly. The errors between visual interpretation and machine classification were mainly caused by the mixing pixels of grass and sandy land due to the low fraction grass cover. It is hard to distinguish the yellow-green grass pixels and yellow sand pixels in visual interpretation.

3.2.2. UAV-derived FVC and ground-derived FVC evaluation

The proposed method was evaluated by the detailed ground measurement dataset included 4832 trees and 18,798 shrubs. The FVC values calculated from the orthomosaic by UAV-HiRAP were compared with that derived from ground measurements at different sample plot sizes. Fig. 6 shows that these UAV-derived FVCs were larger than those ground-derived FVCs at different spatial level, and the variation between UAV-derived FVCs and ground-derived FVCs increased with the decreasing of the side-length of sample plot ($R^2 = 0.726, 0.682, 0.646$ and 0.606, at 100 m, 50 m, 25 m and 12.5 m plot-levels, respectively; $P < 0.001$). The reasons may be: 1) The crown area obtained by ground measurements was not the real size of the canopy projection area because crown shape was assumed as to be elliptical. 2) The ellipse crown model assumed that the crown was closing, while real crown always had air gaps. 3) It is difficult to guarantee no missing plants in a large-scale ground measurement which may cause the ground-based FVC to be smaller than "true value".

Overall, the fractional woody vegetation cover calculated from orthomosaic and those estimated from ground measurements had a stable linear relationship over different spatial scales, as shown in Fig. 6. The slopes and interceptions of linear regressions were similar at the sample plot with side-length of 100 m, 50 m, 25 m and 12.5 m, whose slopes were 0.73, 0.76, 0.79 and 0.77, and interceptions were 4.9, 4.6, 4.2 and 4.5, respectively (Fig. 6). The stable linear relationships between UAV-derived FVC and ground-based FVC at different spatial-levels show that FVC obtained from both methods were reliable and the differences were caused by different measuring methods. In general, UAV-derived FVCs were calculated from the high resolution (0.1 m/pixel) orthomosaic at pixel scale. Compared with the ground measurement, UAV-derived FVCs were more precise than ground-based FVCs.

3.3. An optimization model for sampling design

The differences between real FVC (FVC_0) and measured FVC (FVC_s) in the study area were often caused by sampling number. This difference can be decreased through the increasing of sampling number. The measured FVC_s with the change of sampling number were simulated by Monte Carlo stochastics sampling. There were 9 different sizes of sample plots to be tested, whose side-length is 1 m, 2 m, 5 m, 10 m, 20 m, 25 m, 50 m, 75 m and 100 m, respectively. As shown in Fig. 7, the relationship between measured FVC_s and sampling number (num) followed the power function $dev = a \cdot num^b$ (a, b is constant), which showed a strong significance for all tested side-lengths (all: $R^2 > 0.99$, $p < 0.001$). When the side-length of the sample plot was fixed, the differences (spacing between up/down FVC_s and FVC_0) was rapidly reduced with the increase of the number of sample plots. The minimum number of the sample plots became smaller with the increase of their side-length. The simulation results showed that the sampling number were 447, 382, 273, 194, 129, 110, 61, 38 and 26 for sample plots whose side-length was 1 m, 2 m, 5 m, 10 m, 20 m, 25 m, 50 m, 75 m and 100 m, respectively when deviation values < 5% (which is defined as 5% sampling error threshold value). When the allowed deviation increase, the number of quadrats was reduced significantly. When the deviation values < 10% (which is defined as 10% sampling error threshold value), the sampling number was 109, 95, 69, 49, 33, 28, 16, 10 and 7 for sample plots with 9 corresponding side-lengths. The number of sample plots was reduced significantly, and the average descent rate was 74% for all sample plots. These results demonstrated that lower accuracy expectation of the measurement can effectively reduce the field workload.

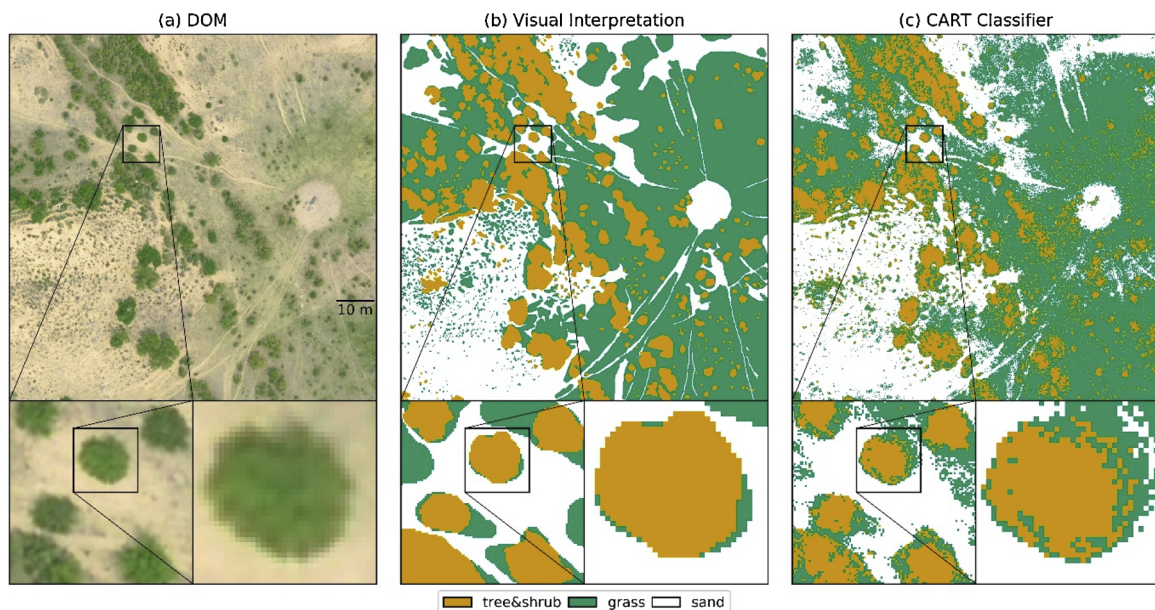


Fig. 5. Visual comparison of vegetation classification between visual interpretation (b) and machine learning (Classification and regression Tree (CART) algorithm) classification (c) on a 100 m × 100 m subplot (a) in the plot of Elm (*Ulmus pumila*) Sparse FOrest Grassland Ecosystem (ESFOGE-Plot).

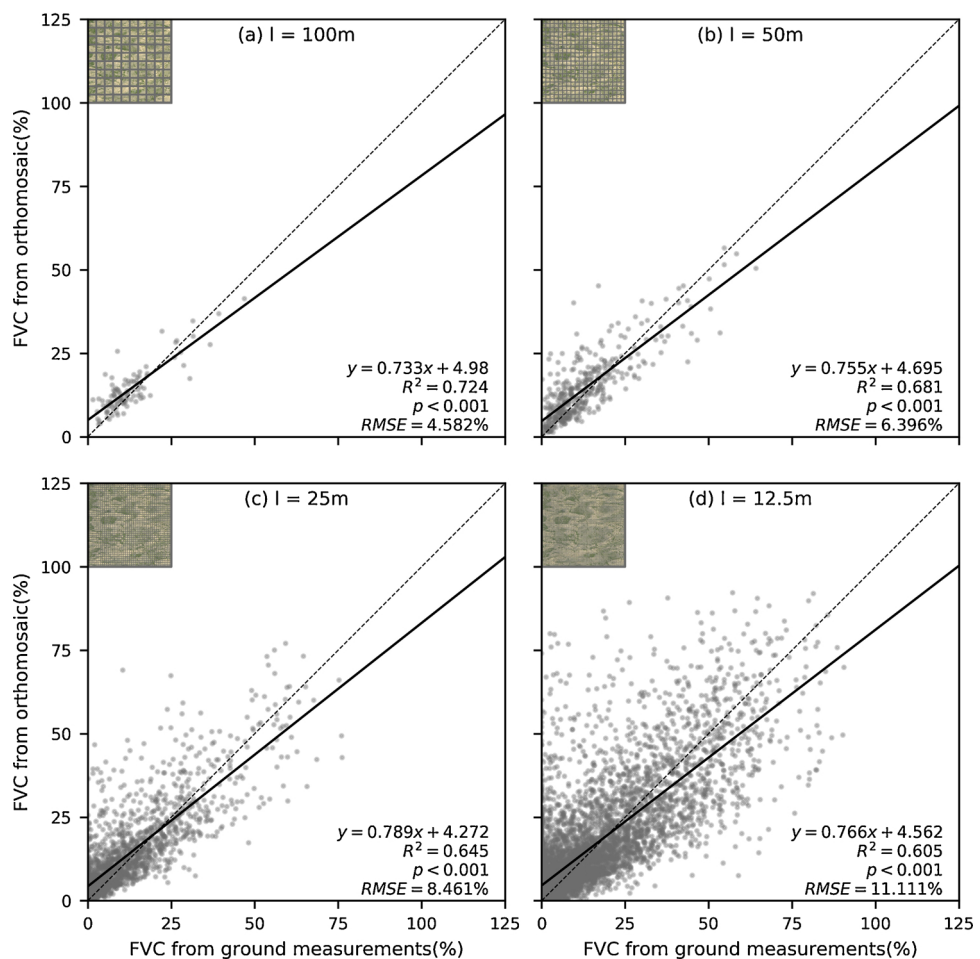


Fig. 6. Comparison between fractional vegetation cover (FVC) derived from ground-derived and UAV-derived FVC calculated from machine classification at the sample plots of four size levels: 100 m × 100 m (a), 50 m × 50 m (b), 25 m × 25 m (c), and 12.5 m × 12.5 m (d). The number of paired quadrat groups were 100, 400, 800, 1600 respectively.

Table 2

The error matrix, overall accuracy (OA), average accuracy (AA) and Kappa coefficient for visual interpretation result and algorithm classification result.

		Visual interpretation			Producer's Accuracy
		Sand	Tree & Shrub	Grass	
Classified	Sand	263492	3213	70263	336968 0.782
	Tree & Shrub	3212	127239	43961	174412 0.730
	Grass	41045	61662	385913	488620 0.790
	Total	307749	192114	500137	1000000 AA = 0.763
User's Accuracy		0.856	0.662	0.772	
Overall Accuracy		0.777			
Kappa Coefficient		0.639			

Derived from the simulated results described above, the relationship between the side-length of quadrats and minimum sampling number at the precision of 90% and 95% of sample estimates was shown in Fig. 8. The side-length and minimum quadrats number follow a power function with a strong significant relationship ($R^2 > 0.99$). This was consistent with the experiences in the field work. The optimizing models can be applied for designing sampling strategy for future field measurements.

4. Discussion

4.1. UAV application in ecology

Using the UAV to explore vegetation status is becoming a new interdisciplinary direction between UAV and vegetation ecology. The UAV offers ecologists a promising, responsive, timely, and cost-effective monitoring method of environmental phenomena at spatial and temporal resolutions which are appropriate to the scales of many ecologically relevant variables (Garcia-Ruiz et al., 2013; Wallace et al., 2017). The UAV remote sensing fills the gaps between ground photogrammetric at small scale and satellite remote sensing with the low spatial resolution. The imagery mosaic technique based on aerial photogrammetry principles and Structure from Motion (SfM) algorithm enables researchers to obtain a fine-scale orthophoto images and 3D point clouds from small digital images (Turner et al., 2012). Some researchers also proved that the image-based FVC estimation has a better accuracy than traditional ground investigation (Chen et al., 2016; McNeil et al., 2016; Rasmussen et al., 2016; Wallace et al., 2016).

The UAV image analysis method is critical for UAV application. Conventional visual interpretation methods are time-consuming and labor intensive for high resolutions UAV images (Cruzan et al., 2016; Hodgson et al., 2016). Recently, the applications of machine learning method in image classification have been increasingly reported in

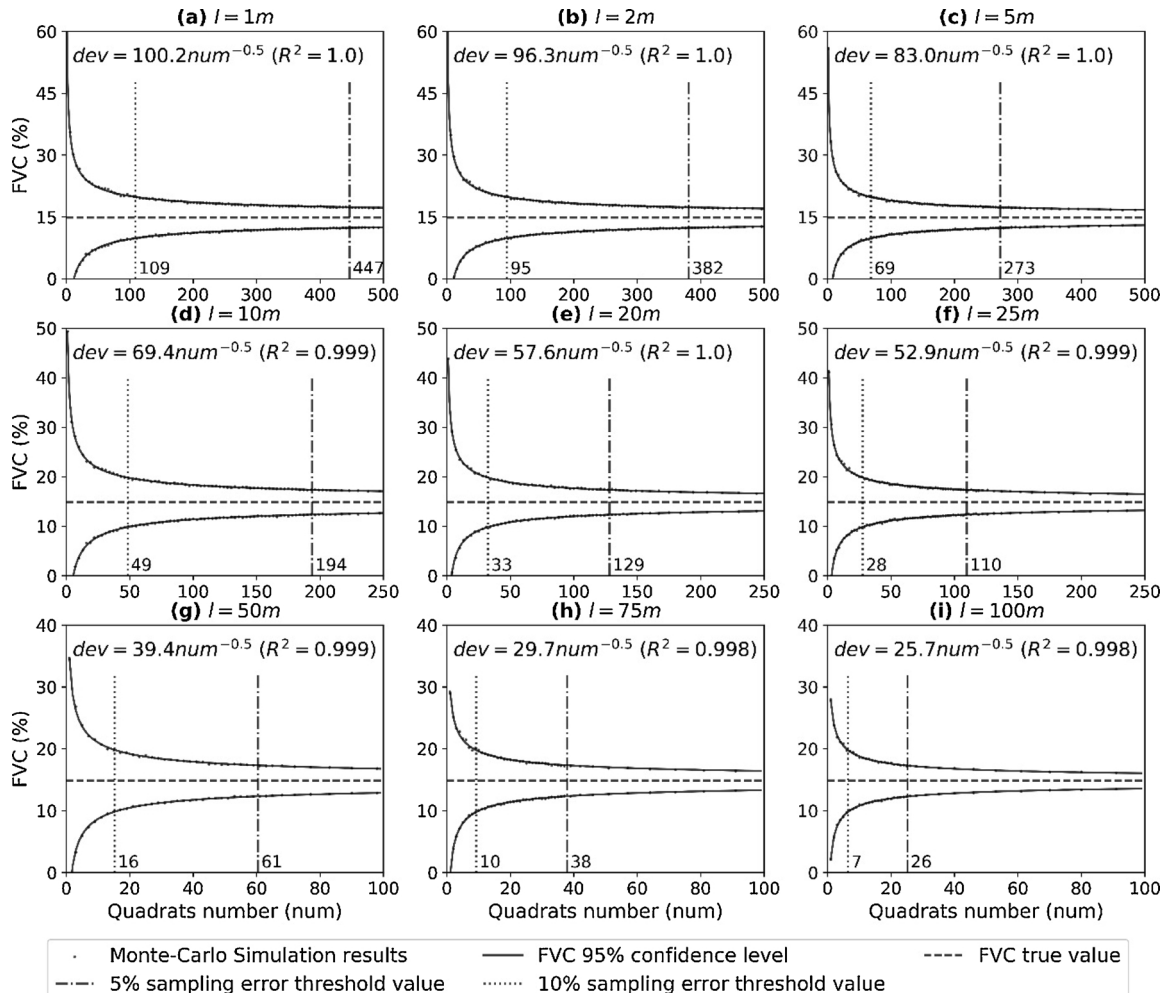


Fig. 7. The sampling error and minimum number of quadrats simulated by Monte Carlo stochastic sampling. FVC calculated from orthomosaic was regarded as the reference value (horizontal dash line). The solid regression lines were the 95% confidence range (mean \pm 2 SD) for different quadrats number (num). The vertical dash line represented the minimum number of quadrats investigated in the field at the accuracy of 90% and 95%.

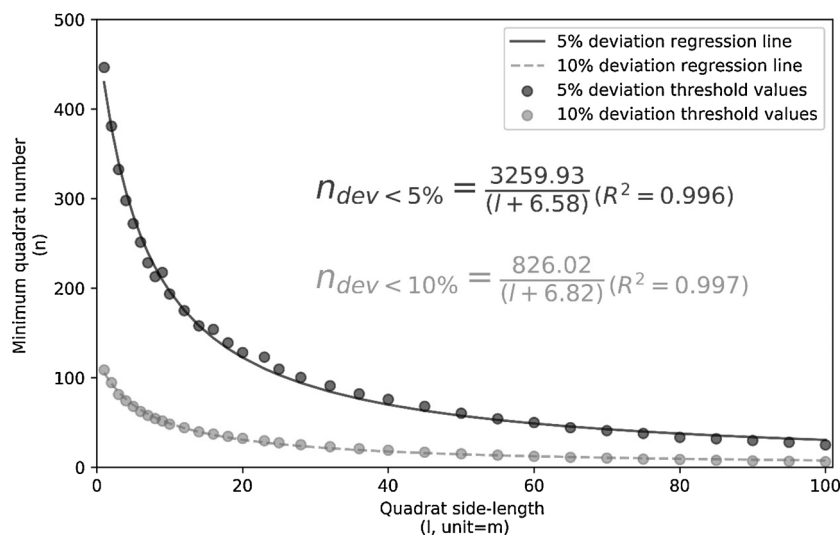


Fig. 8. The relationship between the minimum sampling number and different side-lengths of sample plots when deviation values meet < 10% and < 5% thresholds.

remote sensing studies (Turner et al., 2012; Guo et al., 2013; Feng et al., 2015). Compared with these studies above, the proposed method in this paper is the first attempt to classify woody and herbaceous vegetation and calculate their FVCs at landscape scale ($1 \text{ km} \times 1 \text{ km}$) by using common visible light sensor (RGB channels) based on UAV-derived images. The new method has developed into an interactive web-based software “Unmanned Aerial Vehicles - High Resolution Imagery Analysis Platform” (UAV-HIRAP, <http://www.uav-hirap.org>). It is accessible for researchers to apply the new approach in their study.

4.2. Methods evaluation

The accuracy assessment show that UAV-HIRAP has good overall accuracy, average accuracy, and the Kappa coefficient. Although some studies can achieve higher Kappa coefficients (0.8), the resolution of images used in these studies were lower than current study (Rau et al., 2011, Kappa = 0.87, 5 m; Näsä et al., 2015, Kappa = 0.8, 2 m). Lower spatial resolution results in fewer details and more generality, which is easier to get higher Kappa value. The similar Kappa values were reported in several studies used high resolution image (Feng et al., 2015, Kappa by only RGB = 0.68, 0.07 m; Dash et al., 2017, Kappa = 0.69, 0.3 m).

The proposed method was compared with three popular machine

learning algorithms, i.e. support vector machine (SVM) (Mountrakis et al., 2011), Random Forest (RF) (Yu et al., 2016), Gradient Boost Decision Tree (GBDT) (Friedman, 2001). All these machine learning algorithms showed the similar visual classification performance (Fig. 9) and obtained the similar average accuracy, overall accuracy, and Kappa coefficient (Table 3). However, their computing time costs were very different (Table 3). The proposed method was the least time-consuming, which spent 4 s on training classification model and 185 s on classifying the orthomasics. The efficiency of current method was higher of 166%, 111% and 290% than SVM, RF and GBDT algorithm on the total time-consuming respectively. Overall, the proposed method is more efficient, stable (no random number generator) than other popular machine learning algorithms.

4.3. Implications for sampling design

The reliability of ground investigation is greatly affected by the sampling design (Basu, 1969). The field measurement is time-consuming and labor intensive. In this study, 49 people spent three months on measuring the vegetation structure in 100 ha ESFOGE-Plot. A good sampling strategy can greatly improve the efficiency and accuracy of field investigation. This study found that FVC has great spatial variability in the sparse forest grass land. Our simulation test showed that

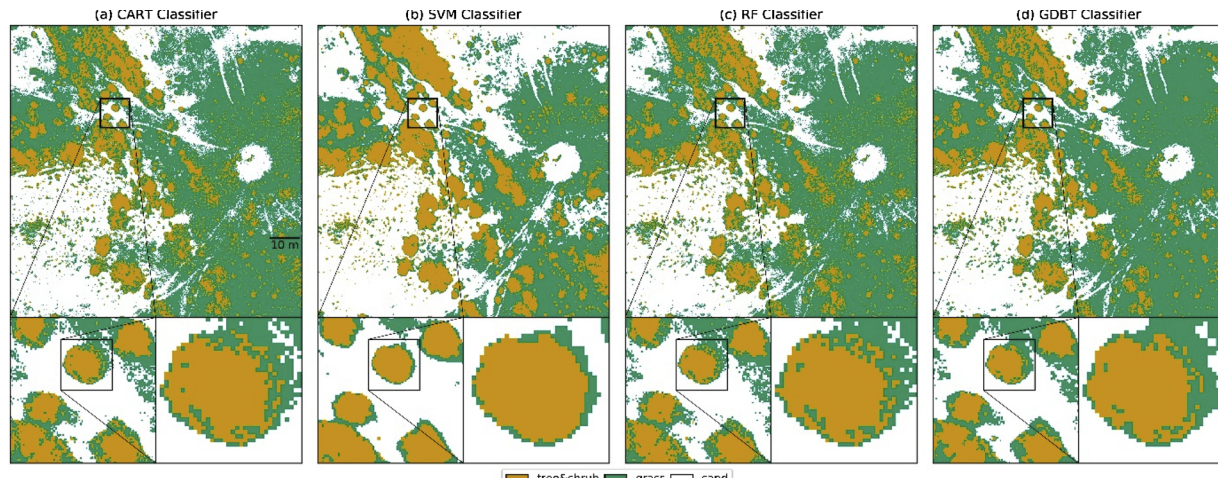


Fig. 9. Visual comparison of vegetation classification by four machine learning algorithms. (a) Classification and Regression Tree (CART); (b) Support Vector Machine (SVM); (c) Random Forest (RF); (d) Gradient Boosting Decision Tree (GBDT).

Table 3

Accuracy assessment and time consuming among four machine learning algorithms.

Algorithm	AA(%)	OA(%)	Kappa	Training	Computing
CART	76.3	77.7	0.6388	4s	185s
SVM	81.3	76.9	0.645	332s	171s
RF	76.9	78.1	0.6465	11s	389s
GBDT	78.1	80.2	0.6776	207s	530s

Note: 1) AA: average accuracy; OA: overall accuracy; Kappa (coefficient) and the time consuming during model training and classification computing;

2) CART: Classification and Regression Tree; SVM: Support Vector Machine; RF: Random Forest; GBDT: Gradient Boosting Decision Tree.

the variability of random sampling FVC was negatively correlated with quadrats area and quadrats number (Fig. 7). Therefore, the trade-off between quadrats number, area and accuracy should concern field ecologist (Picard et al., 2010). It has been proved that large quadrats have a lower per-plot variance while a larger number of small quadrats tend to decrease the standard error of the mean (Evans and Viengkham, 2001). Lin et al. (2013) proved that the variability of basal area decreased with the increasing of quadrats area by using computer simulation and field measurement data. Grussu et al. (2016) pointed out that quadrats area has a significant exponential relationship with coefficient of variance (CV). Our simulation results also showed that there were very good and significant exponential relationships between measured deviation of single quadrat and number for quadrat with specific area (Fig. 7). We further established two optimization models for quadrat area and minimum sampling number which can achieve 90% and 95% precision, respectively (Fig. 8). The required number of quadrats which achieved the specified degree of precision dropped sharply with the increasing of quadrat size. However, the total sampling area increased with the increase of quadrat size, suggesting that using several small quadrats across the sampling area is more efficient than using fewer larger quadrats. Meanwhile, travel time from one quadrat to another should be considered if choosing too many small quadrats (Evans and Viengkham, 2001).

5. Conclusions

This study presented a novel, quick and precise UAV image-based method to detect and map the woody vegetation and herbaceous vegetation and calculate their FVC at landscape level. The proposed method performed more efficient than other popular machine learning algorithm. The developed optimization model for FVC sampling design can optimize the workload of vegetation investigation and to design more efficient sampling strategies. The proposed method was developed to an user-friendly online tool, <http://www.uav-hirap.org>, for the researchers to easily apply this approach in future study. This proposed method also opened up new opportunities for detailed monitoring of important vegetation structural and functional properties (e.g., canopy diameter, tree height, chlorophyll fluorescence) at landscape level.

Author contributions statement

Feng Wang, Qi LU and Yongfei Bai conceived the ideas and designed methodology; Dong Han, Lina Jiang, Xueling Yao and Feng Wang collected the data; Haozhou Wang, Dong Han, Yue Mu, Lina Jiang, Xueling Yao analyzed the data; Haozhou Wang and Feng Wang led the writing of the manuscript. All authors contributed critically to the drafts and gave final approval for publication.

Acknowledgements

We thank 49 volunteers for their assistance with the field measurements. This research was supported by National Key Research and

Development Program of China (Grant No. 2017YFC0503804 and 2016YFC0500801), National Natural Science Foundation of China (Grant No. 31570710) and Chinese Academy of Forestry Science Funds for Distinguished Young Scholar (Grant No. CAFYBB2017QC007).

Appendix A. Supplementary data

Supplementary material related to this article can be found, in the online version, at doi:<https://doi.org/10.1016/j.agrformet.2019.107665>.

References

- Ahlström, A., Raupach, M.R., Schurgers, G., Smith, B., Arneth, A., Jung, M., Reichstein, M., Canadell, J.G., Friedlingstein, P., Jain, A.K., Kato, E., Poultier, B., Sitch, S., Stocker, B.D., Viovy, N., Wang, Y.P., Wiltshire, A., Zaehle, S., Zeng, N., 2015. The dominant role of semi-arid ecosystems in the trend and variability of the land CO₂ sink. *Science* 348, 895–899. <https://doi.org/10.1126/science.aaa1668>.
- Anderson, K., Gaston, K.J., 2013. Lightweight unmanned aerial vehicles will revolutionize spatial ecology. *Front. Ecol. Environ.* 11, 138–146. <https://doi.org/10.1890/120150>.
- Asner, G.P., Martin, R.E., 2009. Airborne spectromics: mapping canopy chemical and taxonomic diversity in tropical forests. *Front. Ecol. Environ.* 7, 269–276. <https://doi.org/10.1890/070152>.
- Asner, G.P., Martin, R.E., Knapp, D.E., Tupayachi, R., Anderson, C.B., Sinca, F., Vaughn, N.R., Ilactayo, W., 2017. Airborne laser-guided imaging spectroscopy to map forest trait diversity and guide conservation. *Science* 355, 385–389. <https://doi.org/10.1126/science.aaj1987>.
- Basu, D., 1969. Role of the sufficiency and likelihood principles in sample survey theory. *Sankhyā Indian J. Stat. Ser* 1961–2002 (31), 441–454. https://doi.org/10.1007/978-1-4419-5825-9_22.
- Bishop, Y.M., Fienberg, S.E., Holland, P.W., 1975. *Discrete Multivariate Analysis: Theory and Practice*. Cambridge, Massachusetts: Massachusetts Institute of Technology Press, New York.
- Breiman, L., Friedman, J.H., Olshen, R.A., Stone, C.J., 1984. *Classification and Regression Trees*. Routledge, New York.
- Chen, J., Yi, S., Qin, Y., Wang, X., 2016. Improving estimates of fractional vegetation cover based on UAV in alpine grassland on the Qinghai-Tibetan Plateau. *Int. J. Remote Sens.* 37, 1922–1936. <https://doi.org/10.1080/0143161.2016.1165884>.
- Congalton, R.G., 1991. A review of assessing the accuracy of classifications of remotely sensed data. *Remote Sens. Environ.* 37, 35–46. [https://doi.org/10.1016/0034-4257\(91\)90048-B](https://doi.org/10.1016/0034-4257(91)90048-B).
- Cook, K.L., 2016. An evaluation of the effectiveness of low-cost UAVs and structure from motion for geomorphic change detection. *Geomorphology* 278. <https://doi.org/10.1016/j.geomorph.2016.11.009>.
- Cruzan, M.B., Weinstein, B.G., Grasty, M.R., Kohrn, B.F., Hendrickson, E.C., Arredondo, T.M., Thompson, P.G., 2016. Small unmanned aerial vehicles (micro-UAVs, drones) in plant ecology. *Appl. Plant Sci.* 4, 1600041. <https://doi.org/10.3732/apps.1600041>.
- Cunliffe, A.M., Brazier, R.E., Anderson, K., 2016. Ultra-fine grain landscape-scale quantification of dryland vegetation structure with drone-acquired structure-from-motion photogrammetry. *Remote Sens. Environ.* 183, 129–143. <https://doi.org/10.1016/j.rse.2016.05.019>.
- Dandois, J.P., Ellis, E.C., 2013. High spatial resolution three-dimensional mapping of vegetation spectral dynamics using computer vision. *Remote Sens. Environ.* 259–276. <https://doi.org/10.1016/j.rse.2013.04.005>.
- Dash, J.P., Watt, M.S., Pearse, G.D., Heaphy, M., Dungey, H.S., 2017. Assessing very high resolution UAV imagery for monitoring forest health during a simulated disease outbreak. *ISPRS J. Photogramm. Remote Sens.* 131, 1–14. <https://doi.org/10.1016/j.isprsjprs.2017.07.007>.
- D'Odorico, P., Caylor, K., Okin, G.S., Scanlon, T.M., 2007. On soil moisture–vegetation feedbacks and their possible effects on the dynamics of dryland ecosystems. *J. Geophys. Res. Biogeosci.* 112. <https://doi.org/10.1029/2006JG000379>.
- Duan, T., Chapman, S.C., Holland, E., Rebetzke, G.J., Guo, Y., Zheng, B., 2016. Dynamic quantification of canopy structure to characterize early plant vigour in wheat genotypes. *J. Exp. Bot.* 67, 4523–4534. <https://doi.org/10.1093/jxb/erw227>.
- Evans, T.D., Viengkham, O.V., 2001. Inventory time-cost and statistical power: a case study of a Lao rattan. *For. Ecol. Manag.* 150, 313–322. [https://doi.org/10.1016/S0378-1127\(00\)00589-2](https://doi.org/10.1016/S0378-1127(00)00589-2).
- Fairman, H.S., Brill, M.H., Hemmendinger, H., 1997. How the CIE 1931 color-matching functions were derived from Wright-Guild data. *Color Res. Appl.* 22, 11–23. [https://doi.org/10.1002/\(SICI\)1520-6378\(199702\)22:1<11::AID-COL4>3.0.CO;2-7](https://doi.org/10.1002/(SICI)1520-6378(199702)22:1<11::AID-COL4>3.0.CO;2-7).
- Faye, E., Rebaudo, F., Yáñez-Cajo, D., Cauvy-Fraunié, S., Dangles, O., 2016. A toolbox for studying thermal heterogeneity across spatial scales: from unmanned aerial vehicle imagery to landscape metrics. *Methods Ecol. Evol.* 7, 437–446. <https://doi.org/10.1111/2041-210X.12488>.
- Feng, Q., Liu, J., Gong, J., 2015. UAV remote sensing for urban vegetation mapping using random forest and texture analysis. *Remote Sens.* 7, 1074–1094. <https://doi.org/10.3390/rs70101074>.
- Filippa, G., Cremonese, E., Migliavacca, M., Galvagno, M., Forkel, M., Wingate, L., Tomelleri, E., Morra di Cellia, U., Richardson, A.D., 2016. Phenopix: a R package for image-based vegetation phenology. *Agric. For. Meteorol.* 220, 141–150. <https://doi.org/10.1016/j.agrformet.2016.01.006>.

- Friedman, J.H., 2001. Greedy function approximation: a gradient boosting machine. *Ann. Stat.* 29, 1189–1232.
- Garcia-Ruiz, F., Sankaran, S., Maja, J.M., Lee, W.S., Rasmussen, J., Ehsani, R., 2013. Comparison of two aerial imaging platforms for identification of Huanglongbing-infected citrus trees. *Comput. Electron. Agric.* 91, 106–115. <https://doi.org/10.1016/j.compag.2012.12.002>.
- Getzin, S., Wiegand, K., Schöning, I., 2011. Assessing biodiversity in forests using very high-resolution images and unmanned aerial vehicles. *Methods Ecol. Evol.* 3, 397–404. <https://doi.org/10.1111/j.2041-210X.2011.00158.x>.
- Grussu, G., Testolin, R., Saulie, S., Farcomeni, A., Yosi, C.K., De Sanctis, M., Attorre, F., 2016. Optimum plot and sample sizes for carbon stock and biodiversity estimation in the lowland tropical forests of Papua New Guinea. *For. Int. J. For. Res.* 89, 150–158. <https://doi.org/10.1093/forestry/cpv047>.
- Guido, van R., 2018. Python (programming language). *Python Software Foundation, US*.
- Guo, W., Fukatsu, T., Ninomiya, S., 2015. Automated characterization of flowering dynamics in rice using field-acquired time-series RGB images. *Plant Methods* 11, 7. <https://doi.org/10.1186/s13007-015-0047-9>.
- Guo, W., Rage, U.K., Ninomiya, S., 2013. Illumination invariant segmentation of vegetation for time series wheat images based on decision tree model. *Comput. Electron. Agric.* 96, 58–66. <https://doi.org/10.1016/j.compag.2013.04.010>.
- Hanbury, A., Serra, J., 2002. A 3D-polar coordinate colour representation suitable for image analysis. *Comput. Vis. Image Underst.* 11, 39.
- Hansen, M.C., Potapov, P.V., Moore, R., Hancher, M., Turubanova, S.A., Tyukavina, A., Thau, D., Stehman, S.V., Goetz, S.J., Loveland, T.R., Kommareddy, A., Egorov, A., Chini, L., Justice, C.O., Townshend, J.R.G., 2013. High-resolution global maps of 21st-Century forest cover change. *Science* 342, 850–853. <https://doi.org/10.1126/science.1244693>.
- Hodgson, J.C., Baylis, S.M., Mott, R., Herrod, A., Clarke, R.H., 2016. Precision wildlife monitoring using unmanned aerial vehicles. *Sci. Rep.* 6. <https://doi.org/10.1038/srep22574>.
- Hoffmann, H., Jensen, R., Thomsen, A., Nieto, H., Rasmussen, J., Friberg, T., 2016. Crop water stress maps for an entire growing season from visible and thermal UAV imagery. *Biogeosciences* 13, 6545–6563. <https://doi.org/10.5194/bg-13-6545-2016>.
- Jeong, S.-J., Schimel, D., Frankenberger, C., Drewry, D.T., Fisher, J.B., Verma, M., Berry, J.A., Lee, J.-E., Joiner, J., 2017. Application of satellite solar-induced chlorophyll fluorescence to understanding large-scale variations in vegetation phenology and function over northern high latitude forests. *Remote Sens. Environ.* 190, 178–187. <https://doi.org/10.1016/j.rse.2016.11.021>.
- Landau, D.P., Binder, K., 2014. *A Guide to Monte Carlo Simulations in Statistical Physics*. Cambridge University Press.
- Leempoel, K., Parisod, C., Geiser, C., Daprà, L., Vittoz, P., Joost, S., 2015. Very high-resolution digital elevation models: are multi-scale derived variables ecologically relevant? *Methods Ecol. Evol.* 6, 1373–1383. <https://doi.org/10.1111/2041-210X.12427>.
- Lin, D., Lai, J., Mi, X., Ren, H., Ma, K., 2013. Spatial variation in community structure of a subtropical evergreen broad-leaved forest: implications for sampling design. *Chin. Sci. Bull.* 58, 1181–1186. <https://doi.org/10.1007/s11434-012-5586-0>.
- Lynch, T.M.H., Barth, S., Dix, P.J., Grogan, D., Grant, J., Grant, O.M., 2015. Ground cover assessment of perennial ryegrass using digital imaging. *Agron. J.* 107, 2347–2352. <https://doi.org/10.2134/agronj15.0185>.
- Malenovský, Z., Lucieer, A., King, D.H., Turnbull, J.D., Robinson, S.A., 2017. Unmanned aircraft system advances health mapping of fragile polar vegetation. *Methods Ecol. Evol.* <https://doi.org/10.1111/2041-210X.12833>.
- McNeil, B.E., Pisek, J., Lepiský, H., Flamenco, E.A., 2016. Measuring leaf angle distribution in broadleaf canopies using UAVs. *Agric. For. Meteorol.* 218–219, 204–208. <https://doi.org/10.1016/j.agrformet.2015.12.058>.
- Mountrakis, G., Im, J., Ogole, C., 2011. Support vector machines in remote sensing: a review. *ISPRS J. Photogramm. Remote Sens.* 66, 247–259. <https://doi.org/10.1016/j.isprsjprs.2010.11.001>.
- Mu, Y., Wang, F., Zheng, B., Guo, W., Feng, Y., 2018. McGET: a rapid image-based method to determine the morphological characteristics of gravels on the Gobi desert surface. *Geomorphology* 304, 89–98. <https://doi.org/10.1016/j.geomorph.2017.12.027>.
- Näsi, R., Honkavaara, E., Lyytikäinen-Saarenmaa, P., Blomqvist, M., Litkey, P., Hakala, T., Viljanen, N., Kantola, T., Tanhuuanpää, T., Holopainen, M., 2015. Using UAV-Based photogrammetry and hyperspectral imaging for mapping bark beetle damage at tree-level. *Remote Sens.* 7, 15467–15493. <https://doi.org/10.3390/rs71115467>.
- Picard, N., Magnusson, S., Banak, L.N., Namkosserena, S., Yalibanda, Y., 2010. Permanent sample plots for natural tropical forests: a rationale with special emphasis on Central Africa. *Environ. Monit. Assess.* 164, 279–295. <https://doi.org/10.1007/s10661-009-0892-y>.
- Poulter, B., Frank, D., Ciais, P., Myneni, R.B., Andela, N., Bi, J., Broquet, G., Canadell, J.G., Chevallier, F., Liu, Y.Y., Running, S.W., Sitch, S., van der Werf, G.R., 2014. Contribution of semi-arid ecosystems to interannual variability of the global carbon cycle. *Nature* 509. <https://doi.org/10.1038/nature13376>.
- Rasmussen, J., Ntakos, G., Nielsen, J., Svensgaard, J., Poulsen, R.N., Christensen, S., 2016. Are vegetation indices derived from consumer-grade cameras mounted on UAVs sufficiently reliable for assessing experimental plots? *Eur. J. Agron.* 74, 75–92. <https://doi.org/10.1016/j.eja.2015.11.026>.
- Rau, J.Y., Jhan, J.P., Lo, C.F., Lin, Y.S., 2011. Landslide mapping using imagery acquired by a fixed-wing uav. *ISPRS - Int. Arch. Photogramm. Remote Sens. Spat. Inf. Sci.* 3822, 195–200. <https://doi.org/10.5194/isprsarchives-XXXVIII-1-C22-195-2011>.
- Reinhard, E., Adhikhmin, M., Gooch, B., Shirley, P., 2001. Color transfer between images. *IEEE Comput. Graph. Appl.* 21, 34–41. <https://doi.org/10.1109/38.946629>.
- Richardson, M.D., Karcher, D.E., Purcell, L.C., 2001. Quantifying turfgrass cover using digital image analysis. *Crop Sci.* 41, 1884–1888. <https://doi.org/10.2135/cropsci2001.1884>.
- Rodriguez-Iturbe, I., D'Odorico, P., Porporato, A., Ridolfi, L., 1999. On the spatial and temporal links between vegetation, climate, and soil moisture. *Water Resour. Res.* 35, 3709–3722. <https://doi.org/10.1029/1999WR900255>.
- Schanda, J., 2007. *Colorimetry: Understanding the CIE System*. John Wiley & Sons.
- Schimel, D.S., 2010. Drylands in the earth system. *Science* 327, 418–419. <https://doi.org/10.1126/science.1184946>.
- Snavely, N., Seitz, S.M., Szeliski, R., 2008. Modeling the world from internet photo collections. *Int. J. Comput. Vis.* 80, 189–210. <https://doi.org/10.1007/s11263-007-0107-3>.
- Turner, D., Lucieer, A., Watson, C., 2012. An automated technique for generating georectified mosaics from ultra-high resolution unmanned aerial vehicle (UAV) imagery, based on structure from motion (SfM) point clouds. *Remote Sens.* 4, 1392–1410. <https://doi.org/10.3390/rs4051392>.
- Wallace, L., Hillman, S., Reinke, K., Hally, B., 2017. Non-destructive estimation of above-ground surface and near-surface biomass using 3D terrestrial remote sensing techniques. *Methods Ecol. Evol.* 8, 1607–1616. <https://doi.org/10.1111/2041-210X.12759>.
- Wallace, L., Lucieer, A., Malenovský, Z., Turner, D., Vopěnka, P., 2016. Assessment of forest structure using two UAV techniques: a comparison of airborne laser scanning and structure from motion (SfM) point clouds. *Forests* 7, 62. <https://doi.org/10.3390/f7030062>.
- Wang, F., 2017. Artificial intelligence in research. *Science* 357, 28–30. <https://doi.org/10.1126/science.357.6346.28>.
- Yu, N., Li, L., Schmitz, N., Tian, L.F., Greenberg, J.A., Diers, B.W., 2016. Development of methods to improve soybean yield estimation and predict plant maturity with an unmanned aerial vehicle based platform. *Remote Sens. Environ.* 187, 91–101. <https://doi.org/10.1016/j.rse.2016.10.005>.
- Zhang, J., Hu, J., Lian, J., Fan, Z., Ouyang, X., Ye, W., 2016. Seeing the forest from drones: testing the potential of lightweight drones as a tool for long-term forest monitoring. *Biol. Conserv.* 198, 60–69. <https://doi.org/10.1016/j.biocon.2016.03.027>.